Non-Negative Iterative Convex Refinement Approach for Accurate and Robust Reconstruction in Cerenkov Luminescence Tomography

Meishan Cai, Zeyu Zhang, Xiaojing Shi, *Graduate Student Member, IEEE*, Junying Yang, Zhenhua Hu, *Member, IEEE*, and Jie Tian, *Fellow, IEEE*

***Abstract*— Cerenkov luminescence tomography (CLT) is a promising imaging tool for obtaining three-dimensional (3D) non-invasive visualization of the *in vivo* distribution of radiopharmaceuticals. However, the reconstruction performance remains unsatisfactory for biomedical applications because the inverse problem of CLT is severely ill-conditioned and intractable. In this study, therefore, a novel non-negative iterative convex refinement (NNICR) approach was utilized to improve the CLT reconstruction accuracy, robustness as well as the shape recovery capability. The spike and slab prior information was employed to capture the sparsity of Cerenkov source, which could be formalized as a non-convex optimization problem. The NNICR approach solved this non-convex problem by refining the solutions of the convex sub-problems. To evaluate the performance of the NNICR approach, numerical simulations and *in vivo* tumor-bearing mice models experiments were conducted. Conjugated gradient based Tikhonov regularization approach (CG-Tikhonov), fast iterative shrinkage-thresholding algorithm based Lasso approach (Fista-Lasso) and Elastic-Net regularization approach were used for the comparison of the reconstruction performance. The results of these experiments demonstrated that the NNICR approach obtained superior reconstruction performance in terms of location accuracy, shape recovery capability, robustness and *in vivo* practicability. It was believed that this study would facilitate the preclinical and clinical applications of CLT in the future.**

***Index Terms*— Cerenkov luminescence tomography, sparse reconstruction, inverse problem, tumor.**

Manuscript received March 19, 2020; revised April 7, 2020; accepted April 9, 2020. Date of publication April 21, 2020; date of current version September 30, 2020. This work was supported by the National Key Research and Development Program of China (2017YFA0205200, 2016YFC0102600), National Natural Science Foundation of China (NSFC) (81930053, 61622117, 81671759, 81227901), the Chinese Academy of Sciences (GJJSTD20170004), the Scientific Instrument Developing Project of the Chinese Academy of Sciences (YZ201672), the Key Research Program of the Chinese Academy of Sciences (KGZD-EW-T03), Beijing Natural Science Foundation (JQ19027), Beijing Nova Program (Z181100006218046), the innovative research team of high-level local universities in Shanghai, and the Zhuhai High-level Health Personnel Team Project (Zhuhai HLHPTP201703). *(Corresponding authors: Zhenhua Hu; Jie Tian.)*

Meishan Cai, Xiaojing Shi, and Zhenhua Hu are with the CAS Key Laboratory of Molecular Imaging, Beijing Key Laboratory of Molecular Imaging, The State Key Laboratory of Management and Control for Complex Systems, Institute of Automation, Chinese Academy of Sciences, Beijing 100190, China, and also with the School of Artificial Intelligence, University of Chinese Academy of Sciences, Beijing 100049, China (e-mail: caimeishan2016@ia.ac.cn; shixiaojing2017@ia.ac.cn; zhenhua.hu@ia.ac.cn).

Zeyu Zhang is with the Engineering Research Center of Molecular and Neuro Imaging of Ministry of Education, School of Life Science and Technology, Xidian University, Xi'an 710071, China (e-mail: zhang.zey.doc@gmail.com).

Junying Yang is with the Department of Hepatobiliary Surgery, Zhujiang Hospital, Southern Medical University, Guangzhou 510280, China (e-mail: yangjy2041@163.com).

Jie Tian is with the CAS Key Laboratory of Molecular Imaging, Beijing Key Laboratory of Molecular Imaging, The State Key Laboratory of Management and Control for Complex Systems, Institute of Automation, Chinese Academy of Sciences, Beijing 100190, China, also with the School of Artificial Intelligence, University of Chinese Academy of Sciences, Beijing 100049, China, also with the Engineering Research Center of Molecular and Neuro Imaging of Ministry of Education, School of Life Science and Technology, Xidian University, Xi'an 710071, China, and also with the Beijing Advanced Innovation Center for Big Data-Based Precision Medicine, School of Medicine, Beihang University, Beijing 100191, China (e-mail: tian@ieee.org).

This article has supplementary downloadable material available at http://ieeexplore.ieee.org, provided by the authors.

Color versions of one or more of the figures in this article are available online at http://ieeexplore.ieee.org.

Digital Object Identifier 10.1109/TMI.2020.2987640

I. Introduction

CERENKOV radiation emerges when a charged particle moves faster than the speed of light in the propagation medium [1]. It can be employed for *in vivo* animal optical imaging as a new imaging modality named Cerenkov luminescence imaging (CLI), first reported in 2009 [2]. Recently, CLI has attracted lots of attention and been widely and successfully used in preclinical and clinical studies, such as tumor detection [3], [4], lymph node visualization [5], biomedical imaging with Cerenkov luminescence endoscopy [6], cancer drug therapy monitoring [7], human thyroid imaging [8] and tumor resection margins assessment [9]. CLI combines the advantages of optical imaging and radionuclide imaging, which is attractive for biomedical applications [10]. There exist lots of clinically available radioisotopes for CLI, such as ^{18}F, ^{64}Cu, ^{68}Ga, ^{89}Zr, ^{90}Y and ^{198}Au [11], which promotes the clinical applications of CLI technology. As a planar imaging modality, CLI could not achieve the depth information and three-dimensional (3D) distribution of radioactive probes [12]. Therefore, Cerenkov luminescence tomography (CLT), a novel 3D optical imaging technique, has been developed by combining the CLI

technology and the 3D anatomical imaging modality [13]. The 3D anatomical imaging modality, such as computed tomography (CT) or magnetic resonance imaging (MRI), provides a spatial outline of the imaging subjects. Based on the outline and Cerenkov luminescence images, the 3D distribution of Cerenkov source is acquired by solving the diffusion equation [14]. It is considered that CLT is a highly promising imaging modality for clinical applications owing to its semi-quantitative analysis capability of *in vivo* radiopharmaceuticals distribution [15].

However, it still remains challenging to acquire satisfactory reconstruction performance of CLT effectively [16]. Most energy of the Cerenkov radiation concentrates in the short wavelength window of the spectrum, which is severely scattered by the biological tissues [17]. Besides that, there also exist plenty of noises in the CLT reconstruction process. The inverse problem of CLT is severely ill-conditioned, resulting in the high complexity of CLT reconstruction. In order to acquire better reconstruction performance, some prior knowledge could be applied to the CLT reconstruction process. It can be divided into three types for the prior knowledge used in the CLT reconstruction, including the animal structure prior, the Cerenkov spectrum prior and the Cerenkov source distribution prior. For the animal structure prior, the first CLT reconstruction for small-animal imaging was conducted with a homogeneous mouse model by assuming that the optical properties were consistent and uniform [13]. Hu *et al.* first employed the different properties of the biological tissues to establish a heterogeneous mouse model, which reduced the systematic error and showed a remarkable improvement of the tumor location accuracy [12]. For the Cerenkov spectrum prior, the multispectral reconstruction method divided the Cerenkov spectrum into several sub-spectral bands to reduce the ill-conditioned level of CLT reconstruction, which improved the reconstruction accuracy comparing to hybrid spectrum method [18]. Based on the multispectral method and the optical characteristics of each sub-spectral band, a more accurate multispectral hybrid method was proposed by Liu et al [19]. Besides that, a modified weight multispectral reconstruction strategy was presented by Guo *et al.*, which greatly improved the reconstruction accuracy and stability [20]. For Cerenkov source distribution prior, the single photon emission computed tomography (SPECT) was used as the prior distribution of the source, which reduced the complexity of CLT [12]. In addition, the sparsity of the Cerenkov source was commonly employed as the prior knowledge, which was often expressed as the regularization method such as L_2-norm regularization (Tikhonov method) [13], L_1-norm regularization (Lasso method) [20] and L_p-norm ($0 < p < 1$) regularization (non-convex method) [21]. However, these methods have their inherent defects and the CLT reconstruction results need to be further improved. L_2-norm regularization was over-smoothed and L_1/L_p-norm regularization was over-sparse, which may decrease the reconstruction accuracy and the shape recovery capability of Cerenkov source. The shape recovery capability of bioluminescence tomography and fluorescence molecular tomography was improved successfully in several related works [22], [23]. It was also significant for CLT to enhance the shape recovery capability of Cerenkov source for analyzing the tumor quantitatively. Recently, Mousavi *et al.* proposed a novel iterative convex refinement (ICR) approach to encourage the sparsity for signal recovery [24]. This work conveyed us a new idea to encourage the sparsity of Cerenkov sources reasonably for sparse reconstruction in CLT, which has the potential to overcome the over-smooth or over-sparse weaknesses in traditional CLT reconstruction approaches. Additionally, since the 3D distribution of Cerenkov source is non-negative in practice, the solution vector of the inverse problem is required to be non-negative as well.

In this study, a novel non-negative iterative convex refinement (NNICR) approach was proposed to improve the CLT reconstruction accuracy, enhance the shape recovery capability and strengthen the reconstruction robustness. For the NNICR approach, the spike and slab prior was utilized to encourage the sparsity, which transformed the inverse problem of CLT into a non-convex optimization problem. A series of non-negative convex problems were solved by the interior-point convex quadratic programming algorithm to approach a sub-optimal solution of the non-convex problem. This iteration process was named as the non-negative iteration convex refinement. The non-negative constraint was designed according to the non-negativity of the Cerenkov source distribution. To our knowledge, this study first introduces the spike and slab prior to the optical reconstruction, and transforms this non-convex problem into a sequence of convex sub-problems. The spike and slab prior could encourage the sparsity of Cerenkov source better and therefore the NNICR approach is expected to obtain the reasonably sparse reconstruction source and improve the CLT reconstruction accuracy as well as the shape recovery capability.

To evaluate the performance of the NNICR approach, numerical simulations and *in vivo* experiments were implemented. Conjugated gradient based Tikhonov regularization approach (CG-Tikhonov) [13], fast iterative shrinkage-thresholding algorithm based Lasso approach (Fista-Lasso) [25] and Elastic-Net regularization approach [16] were used for comparison. Compared with these traditional approaches, the reconstruction results of NNICR showed significant improvement in terms of location accuracy, shape recovery capability, robustness and *in vivo* practicability.

II. Materials and Methods

A. Cerenkov Photon Propagation Model

Absorption and scattering effects exist in the process of Cerenkov photon propagation in biological system, which can be analytically modeled by the radiative transfer equation (RTE). It is nearly impossible to solve the RTE analytically, since it has several interdependent variables. Thus, the RTE is commonly simplified as the diffusion approximation model by assuming that the scattering effect is predominant over the absorption effect in the detectable Cerenkov spectrum used for CLT [21], [26]. The diffusion equation and the Robin boundary condition in CLT can be jointly formulated as [27], [28]:

$$\begin{cases} -\nabla \left[D\left(\boldsymbol{r} \right) \cdot \nabla \Phi \left(\boldsymbol{r} \right) \right] + \mu_a \left(\boldsymbol{r} \right) \cdot \Phi \left(\boldsymbol{r} \right) = S\left(\boldsymbol{r} \right) \\ \Phi \left(\boldsymbol{r} \right) + 2A\left(n \right) \left[\upsilon \left(\boldsymbol{r} \right) \cdot D\left(\boldsymbol{r} \right) \right] = 0, \boldsymbol{r} \in \partial \Omega \end{cases} \tag{1}$$

where ∇ denotes the vector differential operator and $\partial\Omega$ is the boundary of the biological system. $\Phi(\boldsymbol{r})$ is the energy flow per unit area defined as $\Phi(\boldsymbol{r}) = \int_{4\pi} \varphi(\boldsymbol{r}, \hat{s})\, d\Omega \cdot \mu_a(\boldsymbol{r})$ is the absorption coefficient at position $\boldsymbol{r}$. $A(n)$ is a parameter merely depending on the medium refractive index defined as $A(n) = \frac{1+R_f}{1-R_f}$, in which R_f is the inner reflection coefficient. $D(\boldsymbol{r})$ represents the medium diffusion coefficient defined as:

$$D(\boldsymbol{r}) = \frac{1}{3\left[\mu_a(\boldsymbol{r}) + (1-g)\cdot\mu_s(\boldsymbol{r})\right]} \tag{2}$$

in which g is known as the medium anisotropy factor and $\mu_s(\boldsymbol{r})$ is the scattering coefficient. The finite element method (FEM) framework is employed for the discretization of the diffusion equation in CLT such that it can be depicted as the linear equation as:

$$\boldsymbol{A}\boldsymbol{X} = \boldsymbol{\Psi} \tag{3}$$

where $\boldsymbol{A}$ denotes the optical transport system matrix, $\boldsymbol{X}$ is the distribution of optical source and $\boldsymbol{\Psi}$ represents the luminous flux of the vertexes. Actually, the inner vertexes in $\boldsymbol{\Psi}$ and the corresponding rows in $\boldsymbol{A}$ should be removed because only the luminous flux of the surface vertexes can be measured in practice, as follows:

$$\boldsymbol{A}^{\boldsymbol{S}}\boldsymbol{X} = \boldsymbol{\Psi}^{\boldsymbol{S}} \tag{4}$$

where $\boldsymbol{A}^{\boldsymbol{S}}$ is the measured system matrix, $\boldsymbol{\Psi}^{\boldsymbol{S}}$ is the measured vector. Let n_S be the number of surface vertexes, n_V be the number of all vertexes, and thus $\boldsymbol{A} \in R^{n_S \times n_V}$. Using the sparse distribution of radiopharmaceuticals as the prior information, the inverse problem can be formulated as a minimal optimization problem:

$$\begin{aligned} &\min \|\boldsymbol{X}\|_0 \\ &\text{s.t. } \left\|\boldsymbol{A}^{\boldsymbol{s}}\cdot\boldsymbol{X} - \boldsymbol{\Psi}^{\boldsymbol{s}}\right\|_2 < \epsilon \end{aligned} \tag{5}$$

where $\|\boldsymbol{X}\|_0$ denotes the L_0-norm of $\boldsymbol{X}$ and ϵ is a small value.

B. Non-Negative Iterative Convex Refinement for CLT

In this section, a novel NNICR approach was put forward to solve the inverse problem of CLT. Introducing the prior information to capture the sparsity of Cerenkov source distribution was a typical example of optical reconstruction strategies, which could enhance the reconstruction accuracy and robustness in CLT. L_0-norm induced prior is closest to the sparsity definition, but it is a NP-hard problem, which cannot be solved directly. The most widely used examples to express the sparsity are Gaussian prior (L_2-norm minimization) and Laplacian prior (L_1-norm minimization, also known as lasso method). In this study, a novel suitable sparsity promoting prior called as spike and slab prior was induced into the CLT reconstruction, which was widely used in sparse reconstruction and Bayesian inference [29]. The spike and slab prior assumes that every regression coefficient X_i can be modeled as the joint of two densities as:

$$X_i \sim (1-w_i)\,\delta_0 + w_i P_i(X_i) \tag{6}$$

where w_i controls the structural sparsity of the signal and ranges from 0 to 1. δ_0 is the indicator function at zero (spike) and P_i (slab) is a suitable prior distribution for non-zero value of X_i. If w_i is close to zero, X_i tends to remain zero. Since the indicator function is an unbounded Dirac function, any inference from the posterior density for Eq. (6) is ill-defined. Approximation of spike term with a narrow Gaussian function is a commonly used method. The slab term is often defined as a Gaussian function:

$$P_i(X_i) \approx \mathcal{N}\left(0, \sigma^2\lambda^{-1}\right) \tag{7}$$

where $\mathcal{N}(\cdot)$ denotes the Gaussian function and $\sigma^2\lambda^{-1}$ represents the variance of the Gaussian function. Inspired by the Bayesian compressive sensing theory, a hierarchical Bayesian framework is employed to estimate the Cerenkov source distribution, which is precisely formulated as follows [30], [31]:

$$\boldsymbol{\Psi}^{\boldsymbol{S}}|\boldsymbol{A}^{\boldsymbol{S}}, \boldsymbol{X}, \boldsymbol{\gamma}, \sigma^2 \sim \mathcal{N}\left(\boldsymbol{A}^{\boldsymbol{s}}\cdot\boldsymbol{X}, \sigma^2 I\right) \tag{8}$$

$$\boldsymbol{X}|\boldsymbol{\gamma}, \lambda, \sigma^2 \sim \prod_{i=1}^{p} \gamma_i \mathcal{N}\left(0, \sigma^2\lambda^{-1}\right) + (1-\gamma_i)\,\delta_0 \tag{9}$$

$$\boldsymbol{\gamma}|\,\mathbf{k} \sim \prod_{i=1}^{p} \mathcal{B}(\kappa_i) \tag{10}$$

where $\mathcal{B}(\cdot)$ is the Bernoulli distribution and $\boldsymbol{\gamma}$ is the binary indicator variable for every element of $\boldsymbol{X}$. Thus, $X_i = 0$ if γ_i is zero, otherwise X_i follows Gaussian distribution with mean 0 and variance $\sigma^2\lambda^{-1}$. The parameter γ_i controls the sparsity level of $\boldsymbol{X}$ by activating γ_i or not. Based on the *maximum a posteriori* (MAP) theory [32], the optimal $\boldsymbol{X}, \boldsymbol{\gamma}$ are acquired as the following equation:

$$\left(\boldsymbol{X}^*, \boldsymbol{\gamma}^*\right) = \arg max_{\boldsymbol{X},\boldsymbol{\gamma}} \left\{ f\left(\boldsymbol{X}, \boldsymbol{\gamma}|\boldsymbol{A}^{\boldsymbol{S}}, \boldsymbol{\Psi}^{\boldsymbol{S}}, \mathbf{k}, \boldsymbol{\lambda}, \sigma^2\right)\right\} \tag{11}$$

According to related work [24], the MAP estimation problem (11) is equivalent to the following minimization optimization problem:

$$\begin{aligned} \left(\boldsymbol{X}^*, \boldsymbol{\gamma}^*\right) = \arg min_{\boldsymbol{X},\boldsymbol{\gamma}} &\left\|\boldsymbol{\Psi}^{\boldsymbol{S}} - \boldsymbol{A}^{\boldsymbol{S}} * \boldsymbol{X}\right\|_2^2 \\ &+ \lambda\|\boldsymbol{X}\|_2^2 + \sum_{i=1}^{n_V} \rho_i \gamma_i \end{aligned} \tag{12}$$

where ρ_i is a parameter defined as:

$$\rho_i = \sigma^2 \log\left(\frac{2\pi\sigma^2(1-\kappa_i)^2}{\lambda\kappa_i^2}\right) \tag{13}$$

Eq. (12) offers greater generality in capturing sparsity of $\boldsymbol{X}$ and has broad applicability in sparse recovery and image restoration. However, it is a non-convex mixed-integer programming involving the binary indicator variable $\boldsymbol{\gamma}$ and is not easily solvable using traditional convex optimization methods. Several ways are attempted to simplify the optimization problems. Yen *et al.* changes the last term of Eq. (12) to $\rho\|\boldsymbol{X}\|_0$ and the optimization problem is solved by using majorization-minimization algorithm [29]. A relaxation of L_0-norm to L_1-norm will simplify the optimization problem to the widely used Elastic-Net regularization approach. However, these indirect approaches would reduce the accuracy of the solutions. The NNICR is developed to solve Eq. (12) directly to obtain the non-negative Cerenkov source distribution. The central idea of the NNICR approach is to generate a series of

convex optimization sub-problems and refine the solution of previous iteration by solving a modified non-negative convex optimization sub-problem. At iteration n of NNICR, the indicator variable is replaced with the normalized ratio as:

$$\gamma_i^n = \frac{X_i}{\mu_i^{n-1}} \tag{14}$$

where μ_i^{n-1} is the average value of optimal X_i^* obtained from iteration 1 to *n-1* and defined as follows:

$$\mu_i^{n-1} = \frac{1}{n-1}\sum_{k=1}^{n-1} X_i^k \tag{15}$$

$\frac{X_i}{\mu_i^{n-1}}$ is expected to converge to γ_i, if the solution $\boldsymbol{X}$ converges to a point in $\mathbb{R}^{n_V}$. In each iteration, NNICR solves a non-negative convex quadratic programming problem as follows [24]:

$$\boldsymbol{X}^n = \arg min_{\boldsymbol{X}\geq 0} \left\| \boldsymbol{\Psi}^S - \boldsymbol{A}^S \boldsymbol{X} \right\|_2^2 + \lambda \left\| \boldsymbol{X} \right\|_2^2 + \sum_{i=1}^{n_V} \rho_i \frac{X_i}{\mu_i^{n-1}} \tag{16}$$

where $\boldsymbol{X}$ converges to a sub-optimal solution of Eq. (12). At the termination where the solution converges, the final ratio $\frac{X_i^*}{\mu_i^n}$ is equal to zero if $X_i^* = 0$ and converges to 1 if $X_i^* \neq 0$. Hence, the ratio $\frac{X_i}{\mu_i^n}$ matches the value of γ_i in both cases. Therefore, γ_i could be replaced with $\frac{X_i}{\mu_i^n}$ and thus the non-convex problem is changed to a series of convex optimization problems. These sub-problems can be solved by the interior-point convex quadratic programming algorithm [33], [34]. This algorithm using the logarithmic barrier function during minimization, which leads to the intrinsic non-negativity of each sub-problem and the NNICR approach achieves the non-negative reconstruction results finally. More details about the interior-point convex quadratic programming algorithm are provided in the Supplemental Materials. Therefore, the NNICR approach for solving the inverse problem of CLT can be summarized in Algorithm 1. In addition, the convergence analysis of the NNICR approach is also provided in the Supplemental Materials.

Algorithm 1 NNICR Approach for CLT

Preprocess

1) Segment CT data into different tissues.
2) Map the CLI images to the CT data.

Input: Calculate the measured system matrix $\boldsymbol{A}^S$ and measured vector $\boldsymbol{\Psi}^S$.
Initialization: Let $\mu^0 = \left(\boldsymbol{A}^S\right)^T \boldsymbol{\Psi}^S$, iteration index $n = 1$.
Repeat
Step 1: Utilize the interior-point convex quadratic programming algorithm to solve Eq. (16).
Step 2: Update μ_i^n by Eq. (15).
Step 3: Increase iteration index $n = n + 1$.
Until $\left\| \boldsymbol{X}^n - \boldsymbol{X}^{n-1} \right\| \leq tol$.
Output: $\boldsymbol{X}^* = \boldsymbol{X}^{n-1}$.

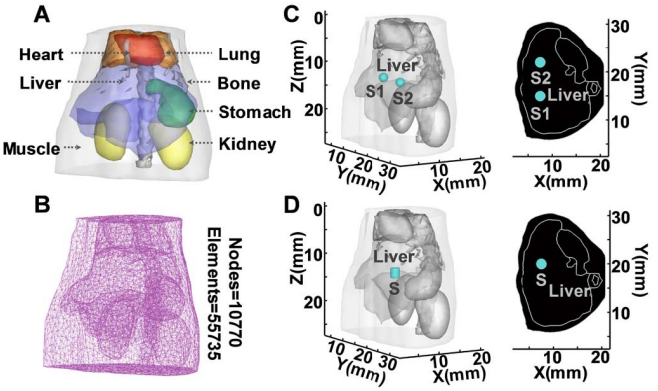

Fig. 1. Numerical simulation settings. (A) The torso section of the digital mouse model used for numerical simulations. (B) The tetrahedral mesh of the digital mouse model applied in the inverse problem of CLT. (C) Two spherical sources (S1 and S2) were implanted into the liver area. (D) Cylindrical source (S) was implanted into the liver area. The 3D view and axial view were displayed.

TABLE I
OPTICAL COEFFICIENTS USED IN THE EXPERIMENTS

Tissues	$\mu_a\,(mm^{-1})$	$\mu_s\,(mm^{-1})$	g
Bone	0.08	37.27	0.93
Heart	0.08	10.07	0.90
Stomach	0.10	17.00	0.90
Liver	0.47	10.00	0.93
Kidney	0.09	23.59	0.90
Lung	0.26	31.56	0.93
Muscle	0.12	15.58	0.97

C. Numerical Simulations

Several numerical simulations based on a heterogeneous digital mouse model [35] were conducted to assess the reconstruction performance of the NNICR approach. CG-Tikhonov, Fista-Lasso and Elastic-Net approaches were used for comparison. More details about the parameter selection process of these approaches were provided in the Supplemental Materials. The torso section of the digital mouse model with a height of 26 *mm* was chosen and divided into seven tissues, including bone, heart, stomach, liver, kidney, lung and muscle (Fig. 1A). The empirical optical properties of different tissues at wavelength 650 *nm* used for all the numerical simulations and *in vivo* experiments were displayed in Table I [21]. The selected torso section of the digital mouse model was discretized into a uniform tetrahedral mesh by Amira 5.2 (Visage Imaging, Australia), which consisted of 10770 mesh nodes and 55735 tetrahedral elements (Fig. 1B) in the reconstruction process. Three simulation experiments were conducted in order to verify the performance of NNICR approach comprehensively. Firstly, the dual-source simulation was designed to evaluate the location accuracy. Secondly, the cylindrical source reconstruction was employed to verify the location accuracy and shape recovery capability. Thirdly, the anti-noise simulation was conducted to test the reconstruction robustness. In addition, CG-Tikhonov approach, Fista-Lasso approach and Elastic-Net approach were used for comparisons. All processes of the

TABLE II
CERENKOV SOURCE SETTINGS IN NUMERICAL SIMULATIONS

Simulation	Source	Center (*mm*)	Intensity	Noise level
Dual-source	S1	(7.5, 15, 12)	1	0
	S2	(7.5, 22, 12)	1	0
Cylindrical	S	(7.5, 20, 12)	1	0
Anti-noise	S	(7.5, 20, 12)	1	10%

simulations were implemented on a personal computer with Intel(R) Core(TM) i7-4790K CPU @ 4.00Hz and 16.0GB RAM.

For the dual-source reconstruction simulation, two spherical sources with a radius of 1 *mm* and the same intensity were implanted in the liver of the digital mouse model (Fig. 1C). The center coordinates of the two sources were (7.5, 22, 12) *mm* and (7.5, 15, 12) *mm,* respectively. Thus, the center-to-center separation between the two sources was 7 *mm*. The sources (S1 and S2) were displayed with blue color in 3D view and axial view. A cylindrical source with a radius of 1 *mm* and a height of 2 *mm* was set inside the mouse abdomen for the second numerical simulation (Fig. 1D). The center of the cylinder was (7.5, 20, 12) *mm*. Furthermore, the cylindrical source implanted mouse was also used for the anti-noise performance test. Gaussian noise with a ratio of 10% was added to the surface flux signals as the noise interference. Each anti-noise test was run three times. The same intensity was set in order to compare the location accuracy, shape recovery capability and anti-noise performance of the proposed algorithm fairly. Summarily, the Cerenkov source settings of all numerical simulations were listed in Table II.

D. In Vivo Experiments

All the experimental female BALB/c nude mice (4-6 *weeks*, 15-20 *g*) were purchased from the Beijing Vital River Laboratory Animal Technology Co. Ltd. All the animal experiments were conducted under the protocols approved by the Institutional Animal Care and Use Committee, Chinese Academy of Sciences. All surgical and imaging procedures were performed under isoflurane gas anesthesia and all efforts were made to reduce the pain of experimental mice. 4T1 breast tumor cells were cultured and employed to establish the 4T1 breast cancer xenografts. The radiotracer [^{18}F]-Fluoro-2-deoxy-d-glucose (^{18}F-FDG) used for *in vivo* experiments was provided by the Department of Nuclear Medicine, Peking University Cancer Hospital, Beijing, China.

In this study, two *in vivo* experiments, including the single-tumor reconstruction and dual-tumor reconstruction, were conducted to verify the performance of the NNICR approach. In the single-tumor reconstruction experiment, 4T1 breast cancer cells ($\sim 1 \times 10^7$) were subcutaneously injected to construct the single breast tumor-bearing mouse. The tumor was allowed to grow for one week. Then, 800±50 μCi ^{18}F-FDG was injected into the tumor-bearing mouse *via* the tail vein under the anesthesia with 2% isoflurane. 40 *min* later, the surface white images and Cerenkov luminescent images were acquired by the electron-multiplying charge-coupled device (EMCCD) of our CLT imaging system after the injected ^{18}F-FDG accumulated to the bladder and tumor [36]. In addition, the micro-CT module achieved the 3D structural images. These images were employed to accomplish the reconstruction of CLT. In the dual-tumor reconstruction experiment, two adjacent breast tumors with a distance of $\sim$10 *mm* were constructed by injecting $\sim 1 \times 10^7$ cells, respectively. Other experimental operations were similar to those of the single-tumor reconstruction. The CLI signal of the bladder area was blocked with a small black cardboard to compare the dual-tumor reconstruction performance. The positron emission tomography (PET) images were obtained to verify the real tumor areas. Lastly, the tumors were taken out from the mice and the hematoxylin and eosin (H&E) stain was performed to verify the property of the resected tissues.

E. Evaluation Metrics

Several evaluation metrics were used to quantify the reconstruction performance. Location error (LE) was used to evaluate the position accuracy. First, weighted location (WL) refers to the reconstructed coordinate obtained by weighting the coordinates of all nodes with reconstructed source energy, which is formulated as follows:

$$WL(\boldsymbol{X}) = \sum_{i=1}^{n} X_i node_i \tag{17}$$

where $node_i = (x_i, y_i, z_i)$ is the coordinate of the *i-th* node, and $\boldsymbol{X}$ is the reconstructed source vector. LE is defined as the distance between the weighted location of the true source and that of the reconstructed source as:

$$LE = \|WL(\boldsymbol{X_r}) - WL(\boldsymbol{X_t})\| \tag{18}$$

where $\boldsymbol{X_r}$ and $\boldsymbol{X_t}$ are the distribution vectors of the reconstructed source and the true source, respectively. Dice coefficient is used to access the overlap level of the reconstructed area and the actual area:

$$Dice = 2\frac{|A \cap B|}{|A| + |B|} \tag{19}$$

where A and B are reconstructed source area and the true source area, respectively. Dice coefficient (DC) reflects the shape similarity degree of two objects, and it ranges from zero to one. The higher Dice coefficient is, the higher shape similarity of two objects is. The root mean square error (RMSE) is used to measure the difference between the true values $\boldsymbol{X}$ and the reconstructed values $\boldsymbol{Y}$ [36]:

$$RMSE = \sqrt{\frac{\sum_{i=1}^{N} (\boldsymbol{X}(i) - \boldsymbol{Y}(i))^2}{N}} \tag{20}$$

where N is the number of samples. Smaller RMSE means that the reconstructed values are closer with the true values.

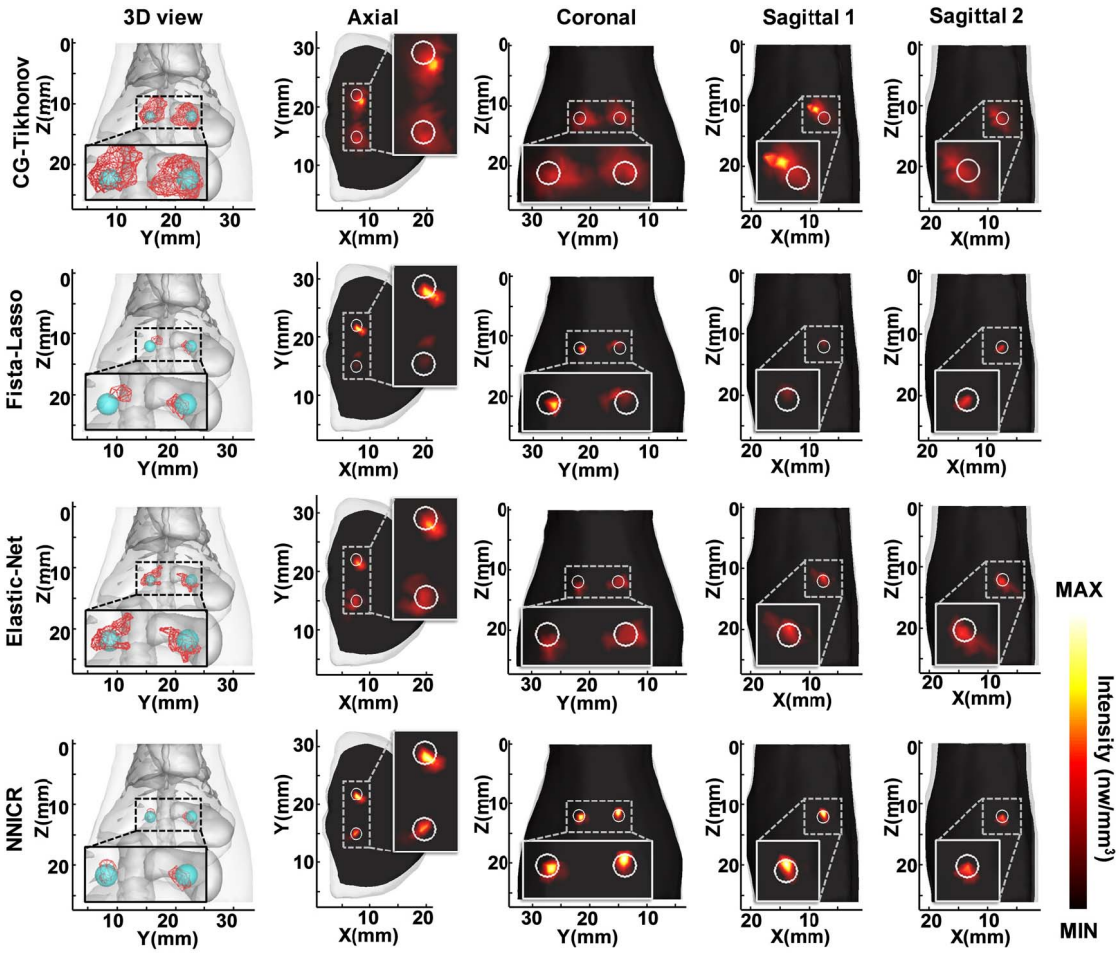

Fig. 2. Results of the dual-source reconstruction. The reconstructed sources using four different approaches were displayed in 3D view, axial view (Z = 12 *mm*), Coronal view (X = 7.5 *mm*) and sagittal view (Y = 15 *mm*, Y = 22 *mm*). The true Cerenkov sources were depicted with blue spheres in the 3D view and white cycles in the slice view. Zoom-in view of the reconstruction results providing a closer look at the distribution of optical signals was put aside the original images.

III. Results

In this section, the reconstruction performance of the NNICR approach was evaluated in terms of location error, shape similarity, robustness and *in vivo* practicability using numerical simulations and *in vivo* experiments. This section shows the results of four experiments, including dual-source reconstruction, cylindrical source reconstruction, anti-noise performance test and *in vivo* reconstruction.

A. Dual-Source Reconstruction

The reconstructed Cerenkov dual spherical sources using different approaches were illustrated in 3D, axial, sagittal and coronal views, respectively (Fig. 2). In 3D view, the actual sources were shown in blue and the reconstructed areas were shown with the red meshes. It is obvious that the center of the 3D mesh reconstructed by the NNICR approach is closer the true sources than other approaches. In slice views, the true Cerenkov source areas were denoted with the white circle or rectangle and the color regions represents the reconstructed Cerenkov source areas by different approaches. It is clearly shown that the reconstructed sources by NNICR approaches are closer to the centers of true sources in all slice views. To analyze the results quantitatively, the LE of S1, S2 and total (S1+S2) and the RMSE were calculated and summarized in Table III. Quantitative analysis demonstrated that the reconstruction result of NNICR had the minimum LE of 0.40 *mm* for S1 and 0.66 *mm* for S2 compared with the other approaches. In addition, the NNICR approach obtained the smallest RMSE of 3.54. NNICR was proved to improve the reconstruction accuracy successfully compared with CG-Tikhonov, Fista-Lasso and Elastic-Net approaches.

TABLE III
Quantitative Comparison in Dual-Source Reconstruction

Method		CG-Tikhonov	Fista-Lasso	Elastic-Net	NNICR
LE (mm)	S1	1.28	1.45	0.42	0.40
	S2	1.09	0.95	0.73	0.66
	Total	2.37	2.40	1.15	1.06
RMSE	\	4.88	4.33	4.05	3.54

B. Cylindrical Source Reconstruction

We compared the reconstruction performance of the NNICR approach with other approaches using the cylindrical source

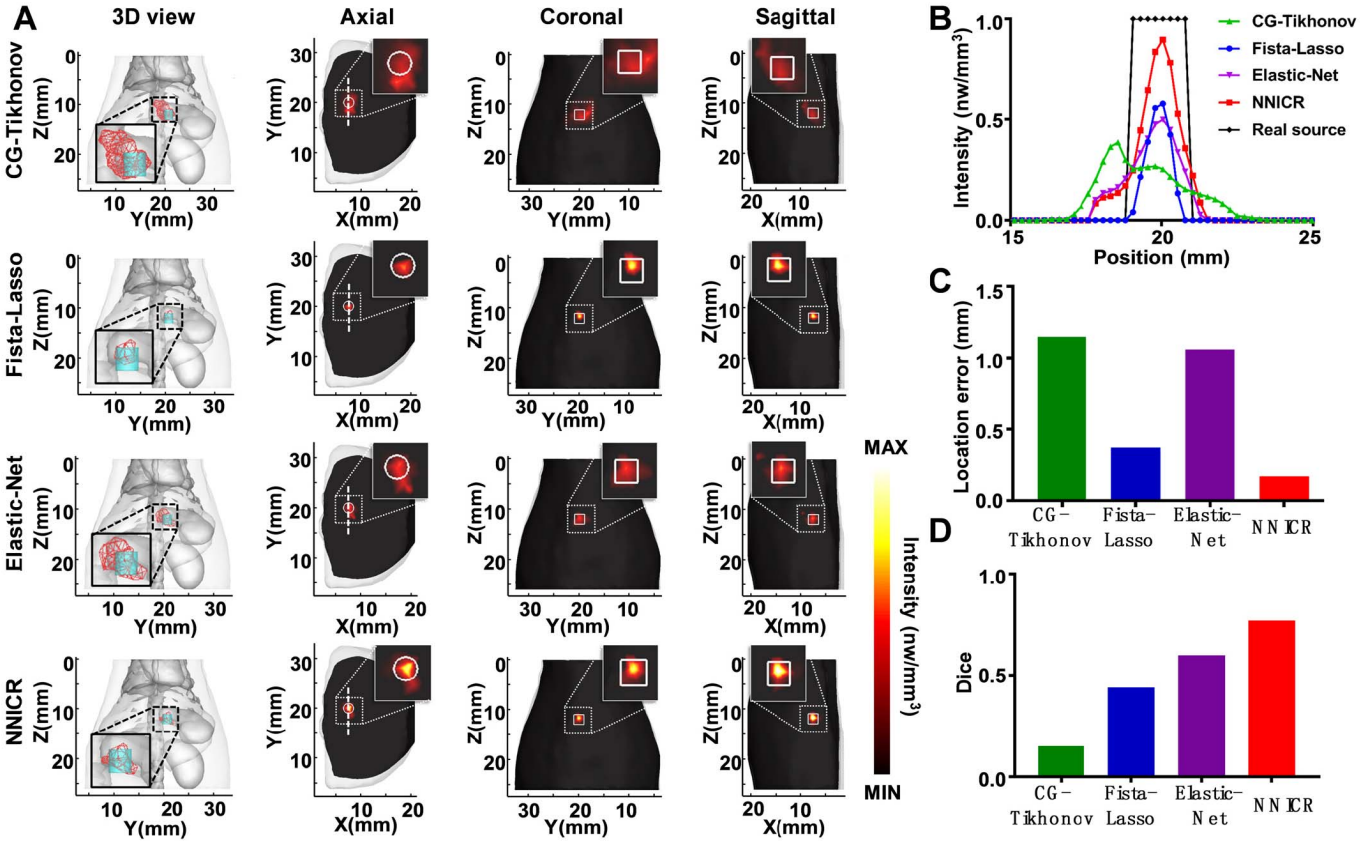

Fig. 3. Results of cylindrical source reconstruction. (A) The reconstructed Cerenkov sources using four different approaches were showed in 3D view, axial view (Z = 12 *mm*), coronal view (X = 7.5 *mm*) and sagittal view (Y = 20 *mm*). Zoom-in view of the reconstruction results providing a closer look at the distribution of optical signals was put aside the original images. (B) The Cerenkov intensity distribution of the reconstruction results along the y-axis of actual Cerenkov source center (the white dotted line in the axial view). (C) The LE of reconstruction results using different approaches. (D) The DC comparison of four approaches.

simulation in terms of the shape recovery capability (Fig. 3). The reconstructed sources were also displayed in 3D, axial, sagittal and coronal views to provide more details (Fig. 3A). It was found that the reconstructed source by NNICR approach was more similar to the true source and had fewer image noises. The 3D mesh of reconstructed source by NNICR had the better overlap with the true source. The Cerenkov intensity distribution of the reconstruction sources along the white dotted line in the axial view also revealed that NNICR approach showed the highest similarity to the true source (Fig. 3B). The quantitative comparison was conducted using LE and DC (Fig. 3C-D). NNICR and Fista-Lasso had much smaller LE compared with CG-Tikhonov and Elastic-Net (Fig. 3C). The LE of NNICR was the least among four approaches. In terms of the shape recovery capability, CG-Tikhonov provided an over-smooth reconstruction, while the reconstruction result of Fista-Lasso was too sparse. The DCs of CG-Tikhonov and Fista-Lasso were 0.15 and 0.44, respectively, smaller than Elastic-Net and NNICR (Fig. 4D). The NNICR approach still offered the best shape recovery capability, with DC of 0.77. Besides that, the RMSE of CG-Tikhonov, Fista-Lasso, Elastic-Net and NNICR were 3.49, 2.63, 2.68 and 1.96, respectively. The NNICR approach obtained the smallest RMSE, indicating that the reconstructed values of NNICR was closer to the true values. The results of cylindrical source reconstruction demonstrated that NNICR approach showed the superiority for the best location accuracy and shape recovery capability.

C. Anti-Noise Performance Test

The effects of Gaussian noise with a level of 10% on reconstruction performance of four approaches were compared and displayed in Fig. 4. Independent simulations were conducted three times for each approach. The reconstructed results of one simulation were shown in 3D and axial view (Fig. 4A). The reconstructed sources deviated from the center of true source more due to the influence of Gaussian noise. The quantitative analysis was expressed as mean ± Standard Deviation (SD). The adding noise in CLT reconstruction increased the LE (Fig. 4B) and reduced the DC (Fig. 4C) for all reconstruction approaches. It was found that NNICR still had the best reconstruction performance with the lowest LE of 0.61 ± 0.023 *mm* and the highest DC of 0.62 ± 0.015. The results of anti-noise performance test revealed that NNICR was robust to the influence of noise.

D. In Vivo Reconstruction

To evaluate the practicability of the NNICR approach for *in vivo* imaging, the *in vivo* CLT reconstruction was conducted

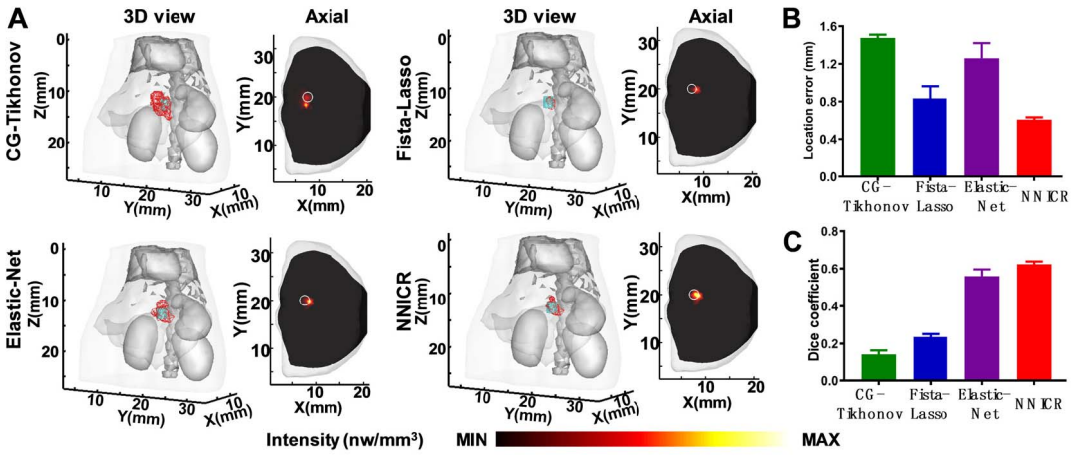

Fig. 4. Results of anti-noise performance test. (A) The reconstructed Cerenkov sources using four different approaches were showed in 3D view and axial view (Z = 12 *mm*). (B) The LE of reconstruction results. (C) The DC of reconstruction results.

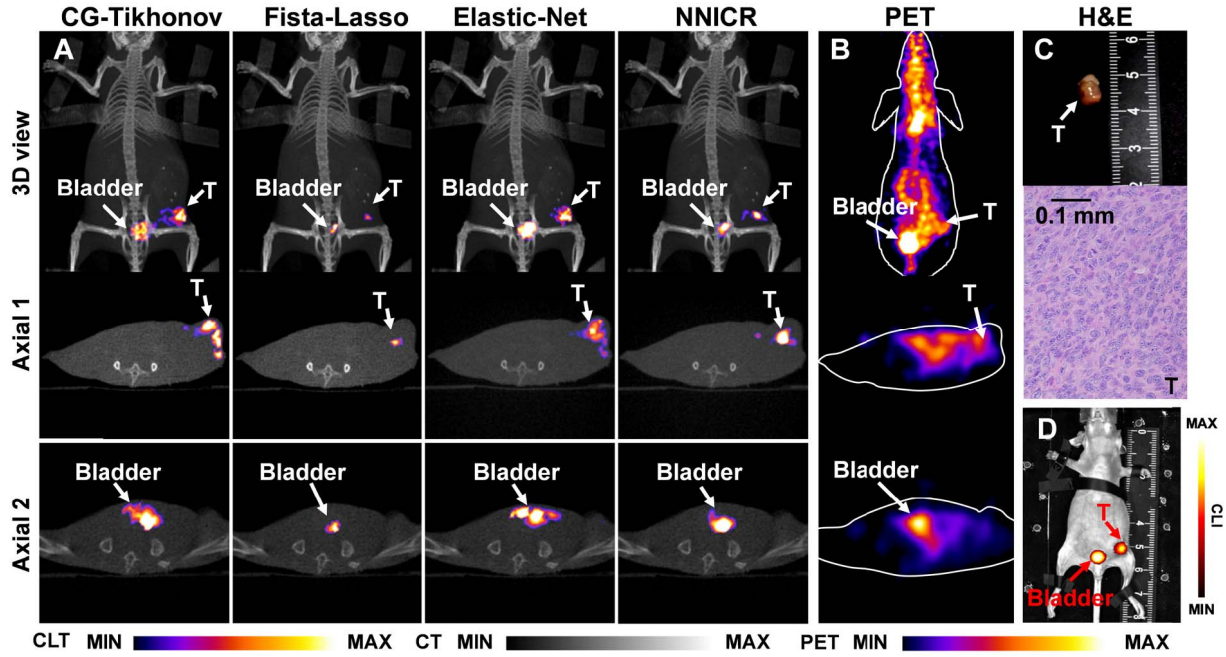

Fig. 5. The single tumor (T) and bladder (Bladder) reconstruction results. (A) The reconstruction results of CG-Tikhonov, Fista-Lasso, Elastic-Net and NNICR were displayed in 3D view and axial slice view. Axial slice 1 showed the tumor area (T), and axial slice 2 showed the bladder area. (B) The results of PET. (C) The photograph of the tumor and its H&E staining results. (D) The obvious signals existed in the CLI results of the tumor and bladder areas.

using the single-tumor and dual-tumor bearing mice. Firstly, the tumor and the bladder was reconstructed and compared in Fig. 5. The reconstructed CLT results (color area) were merged with the CT images and displayed in 3D view and axial slice view, where 'T' and 'Bladder' represented the tumor area and the bladder area, respectively (Fig. 5A). The PET images were shown in 3D and axial views (Fig. 5B). The tumor and bladder were located in two axial slices, respectively. The results of CLI showed that there existed obvious signals in the tumor and bladder areas. Secondly, the process of the dual-tumor reconstruction was similar to that of the single tumor and bladder reconstruction (Fig. 6). Two reconstructed tumors were merged with CT images and the real tumors were represented by T1 and T2 (Fig. 6A). 3D view and axial slice view of PET images were also displayed (Fig. 6B). The sizes and H&E staining images of all tumors were also shown in Fig. 5C and Fig. 6C. Fig. 5D showed that the obvious signals existed in the bladder and tumor areas in the CLI image.

According to the *in vivo* reconstruction results, all the bladder and tumors were successfully reconstructed by four different approaches. However, for CG-Tikhonov and Elastic-Net approaches, the reconstructed results were still over-smooth and had lots of noises. For Fista-Lasso approach, the reconstructed results were too sparse and thus the reconstructed

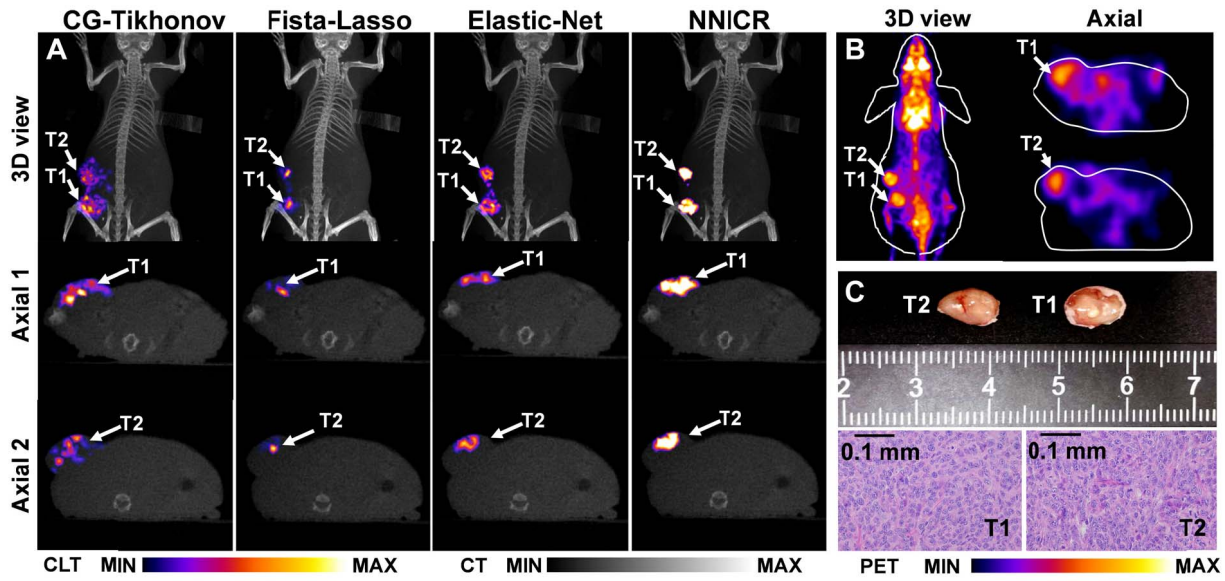

Fig. 6. The dual-tumor (T1 and T2) reconstruction results. (A) The reconstruction results of CG-Tikhonov, Fista-Lasso, Elastic-Net and NNICR were displayed in 3D view and axial slice view. (B) The results of PET. (C) The photograph of the tumors and their H&E staining results.

TABLE IV
COMPARISON OF LOCATION ERROR FOR *in vivo* RECONSTRUCTION (mm)

Approach	T	T1	T2	Mean ± SD
CG-Tikhonov	2.14	1.23	1.65	1.673 ± 0.455
Fista-Lasso	1.68	1.11	1.18	1.323± 0.311
Elastic-Net	1.42	1.53	1.09	1.347 ± 0.229
NNICR	0.93	0.62	0.85	0.800± 0.161

tumors were much smaller than the real tumors. The NNICR-based reconstruction results were compared with the corresponding PET images and the photograph of the tumors. Besides, the centers of the real tumor were roughly estimated by the PET images and the LEs were calculated and listed in Table IV. NNICR approach showed the best accuracy with the least LE. Lastly, the H&E staining results revealed that the reconstructed areas were indeed tumor tissues. The results of *in vivo* reconstruction demonstrated that NNICR approach showed the best practicability for *in vivo* imaging of tumor-bearing mouse.

IV. DISCUSSION AND CONCLUSION

CLT has been considered as a promising imaging modality for 3D visualization of the distribution of radioactive probes inside living animals. But the unsatisfactory reconstruction resulting from the severe ill-conditionedness has limited the biomedical applications of CLT. In this study, a novel NNICR reconstruction method was proposed to achieve better CLT reconstruction performance. First, the optimization function is constructed by using the spike and slab prior to encourage the sparsity of Cerenkov source. Then, the complex non-convex problem can be solved by refining the solution of previous iteration by leveraging a modified non-negative convex problem. Comparing with L_1-norm and L_2-norm regularization, the NNICR approach could control the sparsity of Cerenkov source better based on the prior information generated in the previous iteration. In addition, the non-negative constraint in each iteration also ensures the non-negativity of Cerenkov source, reducing the error and benefiting the CLT reconstruction a lot.

To evaluate the performance of the NNICR approach, numerical simulations and *in vivo* experiments were conducted. CG-Tikhonov, Fista-Lasso, and Elastic-Net were used for qualitative and quantitative comparisons. The experimental results can be concluded as the following. Firstly, the dual-source simulation showed that NNICR approach could improve the location accuracy. Secondly, the cylindrical source simulation revealed that NNICR also had the advantage of source shape recovery capability compared with the conventional approaches. Thirdly, the NNICR approach showed the good robustness in the anti-noise performance test. Lastly, the single-tumor and dual-tumor *in vivo* experiments validated that NNICR showed great practicality for tumor detection of living animals, which demonstrated the potential of NNICR for CLT reconstruction in preclinical researches.

It is also worth mentioning that NNICR encourages the sparsity of Cerenkov source better than conventional approaches. According to the qualitative results of all experiments, CG-Tikhonov approach and Elastic-Net approach generated the over-smoothed solution and Fista-Lasso resulted in the over-sparse solution in CLT reconstruction. These approaches may not be suitable for recovering the shape of the Cerenkov source. NNICR showed the best shape recovery capability with the DC of 0.77. Additionally, it was also interesting

that a reduction in the location error may not increase the Dice coefficient. When the shapes or sizes of two regions differ greatly, the Dice coefficient is small even if the location error is not large. For example, in the dual-source reconstruction simulation, Fista-Lasso approach achieved lower location error and lower Dice coefficient compared with Elastic-Net approach. Besides that, CLT reconstruction results by the NNICR approach had the least noises. These advantages of NNICR would promote its application for CLT reconstruction.

In this study, according to the sparsity of the Cerenkov source, we proposed the NNICR algorithm for CLT reconstruction. The spike and slab prior used in the NNICR approach encouraged the sparsity level of the Cerenkov source better and the convex iterative process could achieve the solution effectively. Therefore, the NNICR approach benefited us to obtain the reasonably sparse reconstruction results of CLT, and thus improved the reconstruction accuracy and enhanced the shape recovery capability of CLT. The results of numerical and *in vivo* experiments validated the effectiveness of the proposed approach. To our knowledge, it was the first time to introduce the spike and slab prior to the optical reconstruction as well. However, although NNICR performed well in CLT reconstruction, it still had some drawbacks. Firstly, the time complexity of NNICR was higher than the comparison approaches. Since NNICR needs to solve a series of non-negative convex problems, it may take several minutes to accomplish one CLT reconstruction with a personal computer. Taking the dual-source reconstruction simulation as an example, the reconstruction times for CG-Tikhonov, Fista-Lasso, Elastic-Net and NNICR were 51.83s, 32.43s, 65.54s and 184.71s, respectively. Therefore, time-consuming is a disadvantage of the NNICR approach. Furthermore, the shape recovery capability of NNICR in *in vivo* experiments was shown only with the qualitative analysis because of the lack of the standard for determining the distribution of tumors in living animals. Even the location error analysis was also a rough result. More quantitative analysis methods for evaluating the results of *in vivo* experiment could be developed in the future. Lastly, the clinical application of CLT based on the NNICR approach deserved further researches in the future.

In conclusion, a novel NNICR approach was proposed to improve the reconstruction performance of CLT in this paper. The NNICR approach is designed according to the combination of the mathematical theory in paper [24] and the physical properties of Cerenkov sources. Compared with several conventional approaches, NNICR performs better in terms of location accuracy, shape recovery capability, robustness and *in vivo* practicability. We believed that this study would promote the preclinical and clinical applications of CLT and facilitate the development of the theoretical study in optical tomography.

Acknowledgment

The authors would like to thank H. Guo and C. Cao for the assistance of the *in vivo* experiments.

References

[1] P. Cerenkov, "Visible luminescence of pure liquids under action of γ-radiation," *Doklady Akad Nauk (USSR)*, vol. 2, pp. 451–454, Aug. 1934.

[2] R. Robertson, M. S. Germanos, C. Li, G. S. Mitchell, S. R. Cherry, and M. D. Silva, "Optical imaging of cerenkov light generation from positron-emitting radiotracers," *Phys. Med. Biol.*, vol. 54, no. 16, pp. N355–N365, Aug. 2009.

[3] D. Fan *et al.*, "^{68}Ga-labeled 3PRGD2 for dual pet and cerenkov luminescence imaging of orthotopic human glioblastoma," *Bioconjugate Chem.*, vol. 26, no. 6, pp. 1054–1060, 2015.

[4] J. P. Holland, G. Normand, A. Ruggiero, J. S. Lewis, and J. Grimm, "Intraoperative imaging of positron emission tomographic radiotracers using cerenkov luminescence emissions," *Mol. Imag.*, vol. 10, no. 3, May 2011, Art. no. 7290.2010.00047.

[5] D. L. J. Thorek *et al.*, "Positron lymphography: Multimodal, high-resolution, dynamic mapping and resection of lymph nodes after intradermal injection of 18F-FDG," *J. Nucl. Med.*, vol. 53, no. 9, pp. 1438–1445, Sep. 2012.

[6] H. Liu *et al.*, "Intraoperative imaging of tumors using cerenkov luminescence endoscopy: A feasibility experimental study," *J. Nucl. Med.*, vol. 53, no. 10, pp. 1579–1584, Oct. 2012.

[7] Y. Xu, E. Chang, H. Liu, H. Jiang, S. S. Gambhir, and Z. Cheng, "Proof-of-Concept study of monitoring cancer drug therapy with cerenkov luminescence imaging," *J. Nucl. Med.*, vol. 53, no. 2, pp. 312–317, Feb. 2012.

[8] A. E. Spinelli *et al.*, "First human cerenkography," *J. Biomed. Opt.*, vol. 18, no. 2, Jan. 2013, Art. no. 020502.

[9] M. R. Grootendorst *et al.*, "Intraoperative assessment of tumor resection margins in breast-conserving surgery using 18F-FDG Cerenkov luminescence imaging: A first-in-human feasibility study," *J. Nucl. Med.*, vol. 58, no. 6, pp. 891–898, 2017.

[10] Z. Hu *et al.*, "*in vivo* nanoparticle-mediated radiopharmaceutical-excited fluorescence molecular imaging," *Nature Commun.*, vol. 6, no. 1, p. 7560, Nov. 2015.

[11] T. M. Shaffer, E. C. Pratt, and J. Grimm, "Utilizing the power of cerenkov light with nanotechnology," *Nature Nanotechnol.*, vol. 12, no. 2, pp. 106–117, Feb. 2017.

[12] Z. Hu *et al.*, "Experimental cerenkov luminescence tomography of the mouse model with SPECT imaging validation," *Opt. Express*, vol. 18, no. 24, pp. 24441–24450, Nov. 2010.

[13] C. Li, G. S. Mitchell, and S. R. Cherry, "Cerenkov luminescence tomography for small-animal imaging," *Opt. Lett.*, vol. 35, no. 7, pp. 1109–1111, Apr. 2010.

[14] X. Ding, K. Wang, B. Jie, Y. Luo, Z. Hu, and J. Tian, "Probability method for cerenkov luminescence tomography based on conformance error minimization," *Biomed. Opt. Exp.*, vol. 5, no. 7, pp. 2091–2112, Jul. 2014.

[15] Z. Hu *et al.*, "Three-dimensional noninvasive monitoring iodine-131 uptake in the thyroid using a modified cerenkov luminescence tomography approach," *PLoS ONE*, vol. 7, no. 5, 2012, Art. no. e37623.

[16] J. Zhong, J. Tian, X. Yang, and C. Qin, "Whole-body Cerenkov luminescence tomography with the finite element SP_3 method," *Ann. Biomed. Eng.*, vol. 39, no. 6, pp. 1728–1735, 2011.

[17] E. Ciarrocchi and N. Belcari, "Cerenkov luminescence imaging: Physics principles and potential applications in biomedical sciences," *EJNMMI Phys.*, vol. 4, no. 1, p. 14, Dec. 2017.

[18] A. E. Spinelli *et al.*, "Multispectral cerenkov luminescence tomography for small animal optical imaging," *Opt. Express*, vol. 19, no. 13, pp. 12605–12618, Jun. 2011.

[19] H. Liu *et al.*, "Multispectral hybrid cerenkov luminescence tomography based on the finite element SPn method," *J. Biomed. Opt.*, vol. 20, no. 8, Aug. 2015, Art. no. 086007.

[20] H. Guo, X. He, M. Liu, Z. Zhang, Z. Hu, and J. Tian, "Weight multispectral reconstruction strategy for enhanced reconstruction accuracy and stability with cerenkov luminescence tomography," *IEEE Trans. Med. Imag.*, vol. 36, no. 6, pp. 1337–1346, Jun. 2017.

[21] H. Guo *et al.*, "Non-convex sparse regularization approach framework for high multiple-source resolution in cerenkov luminescence tomography," *Opt. Express*, vol. 25, no. 23, p. 28068, Nov. 2017.

[22] Y. Gao, K. Wang, S. Jiang, Y. Liu, T. Ai, and J. Tian, "Bioluminescence tomography based on Gaussian weighted laplace prior regularization for *in vivo* morphological imaging of glioma," *IEEE Trans. Med. Imag.*, vol. 36, no. 11, pp. 2343–2354, Nov. 2017.

[23] H. Meng, K. Wang, Y. Gao, Y. Jin, X. Ma, and J. Tian, "Adaptive Gaussian weighted laplace prior regularization enables accurate morphological reconstruction in fluorescence molecular tomography," *IEEE Trans. Med. Imag.*, vol. 38, no. 12, pp. 2726–2734, Dec. 2019.

[24] H. S. Mousavi, V. Monga, and T. D. Tran, "Iterative convex refinement for sparse recovery," *IEEE Signal Process. Lett.*, vol. 22, no. 11, pp. 1903–1907, Nov. 2015.

[25] A. Beck and M. Teboulle, "A fast iterative shrinkage-thresholding algorithm for linear inverse problems," *SIAM J. Imag. Sci.*, vol. 2, no. 1, pp. 183–202, Jan. 2009.

[26] J. Zhong, C. Qin, X. Yang, S. Zhu, X. Zhang, and J. Tian, "Cerenkov luminescence tomography for *in vivo* radiopharmaceutical imaging," *Int. J. Biomed. Imag.*, vol. 2011, Apr. 2011, Art. no. 641618.

[27] W. Cong *et al.*, "Practical reconstruction method for bioluminescence tomography," *Opt. Express*, vol. 13, no. 18, pp. 6756–6771, 2005.

[28] Y. Lv *et al.*, "A multilevel adaptive finite element algorithm for bioluminescence tomography," *Opt. Express*, vol. 14, no. 18, pp. 8211–8223, 2006.

[29] T.-J. Yen, "A majorization–minimization approach to variable selection using spike and slab priors," *Ann. Statist.*, vol. 39, no. 3, pp. 1748–1775, Jun. 2011.

[30] H. Ishwaran and J. S. Rao, "Spike and slab variable selection: Frequentist and Bayesian strategies," *Ann. Statist.*, vol. 33, no. 2, pp. 730–773, Apr. 2005.

[31] M. R. Andersen, O. Winther, and L. K. Hansen, "Bayesian inference for structured spike and slab priors," in *Proc. Adv. Neural Inf. Process. Syst.*, 2014, pp. 1745–1753.

[32] U. Srinivas, Y. Suo, M. Dao, V. Monga, and T. D. Tran, "Structured sparse priors for image classification," *IEEE Trans. Image Process.*, vol. 24, no. 6, pp. 1763–1776, Jun. 2015.

[33] B. Morini and V. Simoncini, "Stability and accuracy of inexact interior point methods for convex quadratic programming," *J. Optim. Theory Appl.*, vol. 175, no. 2, pp. 450–477, Nov. 2017.

[34] S. Boyd, and L. Vandenberghe, *Convex Optimization*. Cambridge, U.K.: Cambridge Univ. Press, 2004.

[35] B. Dogdas, D. Stout, A. F. Chatziioannou, and R. M. Leahy, "Digimouse: A 3D whole body mouse atlas from CT and cryosection data," *Phys. Med. Biol.*, vol. 52, no. 3, pp. 577–587, Feb. 2007.

[36] M. Liu *et al.*, "*in vivo* pentamodal tomographic imaging for small animals," *Biomed. Opt. Express*, vol. 8, no. 3, pp. 1356–1371, Mar. 2017.